Physica B 599 (2020) 412431

Contents lists available at ScienceDirect

Physica B: Physics of Condensed Matter

journal homepage: http://www.elsevier.com/locate/physb

Dysprosium-substitution-induced structural changes of multiferroic nanocrystalline bismuth ferrite and the investigation through positron annihilation and other studies

Jincemon Cyriac [a,b], Saji Augustine [a,b,*], Nandakumar Kalarikkal [c], Shubharaj Mukherjee [d], Maudud Ahmed [d], P.M.G. Nambissan [d]

[a] Department of Physics, St. Thomas College, Arunapuram, Palai, Kottayam, Kerala, 686574, India
[b] Department of Physics, Deva Matha College, Kuravilangad, Kottayam, Kerala, 686633, India
[c] International and Inter University Centre for Nanoscience and Nanotechnology, School of Pure and Applied Physics, Mahatma Gandhi University, Kottayam, Kerala, 686560, India
[d] Applied Nuclear Physics Division, Saha Institute of Nuclear Physics, Kolkata, 700064, India

ARTICLE INFO

Keywords:
Multiferroics
Defects
Electron microscopy
Optical absorption
Positron annihilation spectroscopy
Magnetoelectric coupling

ABSTRACT

This study focuses on the effects of substitution of Bi^{3+} ions in bismuth ferrite ($BiFeO_3$) nanocrystals by dysprosium (Dy^{3+}) ions with special emphasis on the role of defects on its physical properties. X-ray diffraction studies showed a structural transformation from the distorted rhombohedra (*R3c*) to stable orthorhombic (*Pnma*) phase at Dy^{3+} concentration $x = 0.15$–0.20, although no strain was involved as the ionic radii of Dy^{3+} (0.92 Å) is smaller than that of Bi^{3+} (1.17 Å). The crystallite sizes, unit cell volume and the band gap energies reduced with increase in x whereas the dielectric constant drastically increased at $x = 0.2$. A strong magneto electric coupling is also observed. Positron lifetime and coincidence Doppler broadening studies gave clear indications of the transformation at $x = 0.2$ and further indicated that vacancy type defects can be used as tools to identify the structural property changes during cationic substitution.

1. Introduction

Magnetoelectric multiferroics are the materials which exhibit two or more ferroic order parameters like ferroelectricity, ferro-/antiferro-magnetism and ferroelasticity in the same phase [1,2]. Apart from the curiosity to explore the novelties of their crystal structure and electronic properties, they also have attracted enormous research interest due to their potential applications in the areas of technology such as in transducers, actuators, sensors and spintronics devices [3–6]. In all these cases, their basic character as a system to handle high electrical current and strong magnetic fields has been the most important factor of consideration and the efforts to improve these aspects had been continuously undertaken by researchers. The coupling between magnetic and ferroelectric degrees of freedom in multiferroics can produce a number of attractive phenomena such as magnetoelectric (ME) effect in which magnetization can be tuned by the applied electric field and vice versa [7]. Among the most commonly investigated multiferroic compounds, bismuth ferrite ($BiFeO_3$) has been the most popular one due to its favorable properties, a paradigm owing to its potential in the novel functional devices. It has a high Curie temperature T_C ~1103 K and a high Neel temperature T_N ~643 K, both well above room temperature [7,8]. It exhibits a rhombohedrally distorted perovskite (ABO_3) crystal structure with space group *R3c* and lattice parameters $a = b = 5.58$ Å and $c = 13.87$ Å [7–9].

In addition to the magnetoelectric applications, $BiFeO_3$ also has got utilities in other areas of research interest like as a photocatalytic compound due to its small band gap [10,11]. Despite the drawback of suffering from high leakage current, $BiFeO_3$ has been a promising candidate material for continued applications in these areas. However, the suitability of undoped $BiFeO_3$ in many cases becomes constrained as a result of its spiral modulated spin structure (SMSS). Before being considered for applications in multiferroic devices, it should be made possible for $BiFeO_3$ to get rid of its demerits such as large dielectric loss, high leakage current, small remnant polarization, inhomogeneous magnetic spin structure and formation of different impurity phases. Still, the most severe disadvantage in its utility for practical purposes is the

* Corresponding author. Department of Physics, St. Thomas College, Arunapuram, Palai, Kottayam, Kerala, 686574, India.
E-mail address: saji.augustine@devamatha.ac.in (S. Augustine).

https://doi.org/10.1016/j.physb.2020.412431
Received 31 March 2020; Received in revised form 27 July 2020; Accepted 2 August 2020
Available online 8 August 2020

high leakage current [12]. Thus, in order to overcome these hindrances, achieve superior multiferroic properties, reduce leakage current and modify its spatially inhomogeneous spin-modulated incommensurate structure, substitution of anions in parts by those of foreign elements has been considered as an efficient and viable method and the associated physical phenomena had been carefully examined with deep interest. Several attempts have been made by substituting Bi and Fe with rare-earth and transition metal elements [13–15]. In fact, the potential applications of multiferroic $BiFeO_3$ in the field of information storage technology by manoeuvring the inherent magnetic and ferroelectric properties using dopants have opened up new areas of research and technological advancement. It is often realized that substitution is a very effective method of molding the properties of a material for making it better adoptable for various physical and practical applications. Enhanced multiferroicity of the parent material had been achieved by substituting Bi^{3+} by ions such as Gd^{3+}, Sc^{3+}, La^{3+}, Eu^{3+}, Nd^{3+} etc. or by simultaneous substitution of Bi and Fe in $BiFeO_3$ by ions of lanthanides and transition elements [13–17].

Defects are inherent in solid systems due to a number of preparatory and thermodynamic conditions as well as because of the non-stoichiometric composition arising out of several key factors such as the purity of the reagents and the temperature of synthesis. They play a very influencing role on many of the properties even at the atomic scale. Defects like vacancies and interstitials and clusters involving them can result from factors such as charge imbalance, mismatch of ionic radii and lattice parameter variations. Positron annihilation spectroscopy is an indispensable tool in this context as its potential for defect characterization is superior to any other investigatory probe and the success of such investigations has been proved by the results reported in a number of similar studies in the past [18,19]. This report presents the findings of a study related to defects-related variations in the structure and properties of dysprosium (Dy^{3+})-doped $BiFeO_3$ through positron lifetime and coincidence Doppler broadening spectroscopic (CDBS) measurements and aided by complementary evidences from other related and available techniques.

2. Experimental procedure

Dysprosium-doped $BiFeO_3$ samples, of the common nomenclature $Bi_{1-x}Dy_xFeO_3$ ($x = 0$, 0.05, 0.1, 0.15, 0.2, 0.25, 0.3), were synthesized by the sol-gel method using high purity (>99.9%) reagents. Stoichiometric amounts of bismuth nítrate $Bi(NO_3)_3.5H_2O$ dissolved in concentrated HNO_3 acid and ferric nitrate $Fe(NO_3)_2.9H_2O$ and dysprosium nítrate $Dy(NO_3)_3.xH_2O$ dissolved in double distilled water were mixed and sonicated. Poly vinyl alcohol (PVA) of weight equal to the weight of the metal ions (Bi^{3+}, Fe^{3+} and Dy^{3+}) was then added to the mixed solution and stirred for 12 h until it got fully dissolved. Thereafter, the solution was evaporated at 333K for 6–7 days till it gradually turned into a viscous sol and then to a dark brown gel. The final dried gel was calcined at 873K for 2 h. Similar procedure was repeated for the synthesis of the other compounds, the difference being the change in the molarity of the precursor solutions and the weight of the PVA to keep the stoichiometry and nanocrystalline nature of the sample [18,20].

The crystal structures of the samples were studied by X – ray diffraction (XRD) using a Miniflex – Rigaku diffractometer with Cu-*K*α radiation ($\lambda = 1.54$ Å). The data used for the analysis were collected over the range $2\theta = 20^0$-80^0 with a scan step of 0.5° s^{-1}. The morphologies of the samples were examined using a JEOL JEM2100 transmission electron microscope operated at 200 kV and the average particle sizes were found by using the *IMAGE J* software. The elemental compositions of the samples were investigated through energy dispersive X-ray spectroscopy (EDS) using Oxford XMX N device coupled to a JEOL Model JSM-6390LV scanning electron microscope. The UV–Vis absorption spectra of all the samples were recorded by the diffuse reflection spectroscopic method using a JASCO V-670 UV–Vis–NIR spectrophotometer. Dielectric measurements were done on silver coated pellets using an impedance analyser (Agilent - E4980A). Conventional magneto-electric measurements have been carried out using a lock-in amplifier method using a MARINE INDIA *M–E* coupling coefficient measurement device.

Positron annihilation spectroscopic (PAS) studies were performed on the powdered samples using the radioactive isotope ^{22}Na, which is a positron source since it decays by β^+ emission. The source used in this case had strength of approximately 10 μCi and it was deposited within a folded Ni foil. The source was kept immersed within the powder taken in a glass tube. To ensure the capture and annihilation of all the positrons within the sample, the thickness of the powdered sample column had been made sufficiently large and, to remove air and other atmospheric gases getting trapped inside the powder, the glass tube along with the source-sample arrangement had been evacuated to pressure $\sim 10^{-3}$ mbar during the experiments. The positron lifetime measurements were carried out using two barium fluoride (BaF_2) scintillators coupled with XP2020Q photomultiplier tubes whereas, in CDBS measurements, high purity germanium (HPGe) detectors were used to record the annihilation gamma (γ) rays emerging in opposite directions. The time resolution of the slow-fast gamma-gamma coincidence spectrometer performing the positron lifetime measurements was approximately ~0.200 ns (full width at half maximum of the coincidence spectrum of gamma rays from ^{60}Co source). The positron lifetime data were analyzed using the well-known PALSfit program [21]. A three-component fit produced satisfactory results for the spectra of all the samples, with the reduced chi-square confined within 1.05 ± 0.15 [21]. The HPGe detectors used for CDBS measurements had energy resolutions of ~1.3 keV at the annihilation gamma ray energies and the details of analysis of the spectra are discussed later.

3. Results and discussion

3.1. X-ray diffraction analysis

Fig. 1(a)-(g) show the XRD patterns of the $Bi_{1-x}Dy_xFeO_3$ ($x = 0$–0.30) samples. For the precise identification and understanding of the peaks and the phases concerned, we have carried out detailed Rietveld analysis of the data and the results are displayed in the figures. (The goodness of the fit (GOF), as shown in Table 1, differed in the different cases and, for the patterns of the samples with $x = 0.3$, the best we could get was 9.9.) For the pure BFO sample ($x = 0$, Fig. 1(a)), the diffraction planes are indexed to the rhombohedral structure with *R3c* space group (ICDD card no: 01-086-1518). No impurity phases are detected and the lattice parameters are obtained as $a = b = 5.5717$ Å and $c = 13.8637$ Å, which agreed well with the $BiFeO_3$ (*R3c*) structural details available with ICDD card no. 01-086-1518. During the initial doping by Dy^{3+}, i.e., for $x = 0.05$ and 0.1, peaks corresponding to impurity phases of Bi- and Fe-rich $Bi_2Fe_4O_9$ (*Pbam*) (ICDD card no. 01-072-1832) and Bi_2O_3 (*C-4b2*) (ICDD card no. 01-074-2351) are found. At $x = 0.05$, 0.1 and 0.15 only, $Bi_2Fe_4O_9$ (*Pbam*) phase is present and this non-perovskite phase completely vanished in samples with concentration beyond this value (see Fig. 1(e)–(g)). In fact, the percentage of these impurity phases decreased with Dy^{3+} doping from $x = 0.05$ to 0.15. Interestingly, for $x = 0.15$, we obtained the best fit (GOF = 2.35) where the rhombohedral structure with *R3c* space group was considered the most appropriate. The various phases identified from the spectra of the different samples are summarized in Table 1.

Further increase in Dy^{3+} concentration is found to result in the formation of the Dy_2O_3 (*Ia-3*) (ICDD card no: 00-043-1006) phase at $x = 0.20$, 0.25 and 0.3 as indicated in Fig. 1(e)–(g). Substitution of Bi^{3+} ions by larger concentrations of Dy^{3+} ions also caused the formation of $DyFeO_3$ (*Pnma*) phase (ICDD card no: 01-089-6645) in samples of $x = 0.25$ and 0.3. It is also clear that the two separate peaks (104) and (110) in the 2θ range 31^0-33^0 overlap and broaden with increase in Dy^{3+} content and it suggests the occurrence of transformation from the rhombohedral (*R3c*) structure to orthorhombic (*Pnma*) one at $x \geq 0.15$ [22,23].

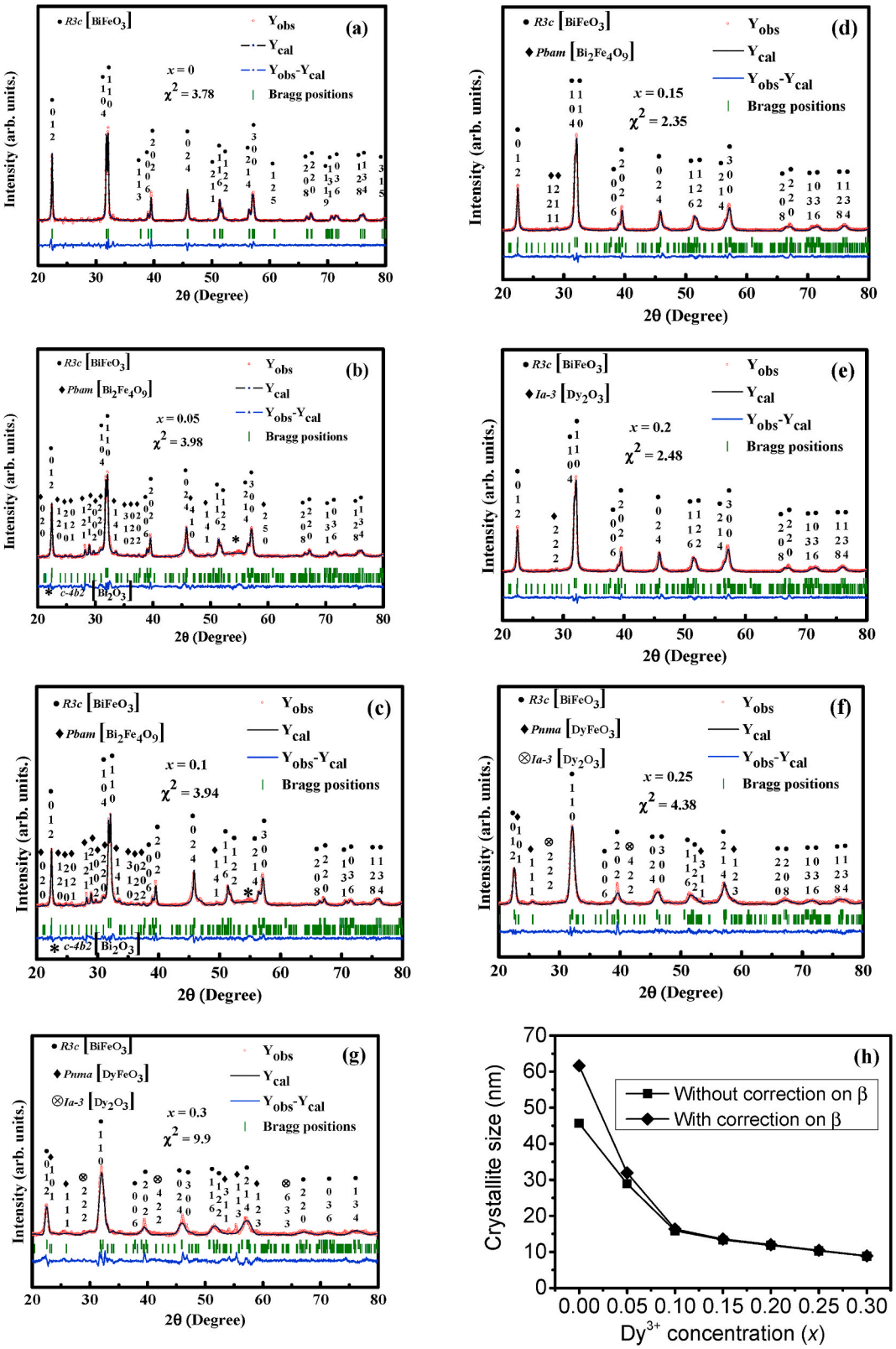

Fig. 1. (a)–(g). XRD patterns including the Rietveld analysis of the $Bi_{1-x}Dy_xFeO_3$ (x = 0, 0.05, 0.1, 0.15, 0.2, 0.25 and 0.3) samples. Fig. 1(h) shows the average crystallite sizes of estimated from the X-ray diffraction peak widths.

The substitution of Bi^{3+} ions by Dy^{3+} ions with smaller radius results in the decrease of the A-site radius and the tolerance factor (t), defined as

$$t = (< r_A > + r_O) / 2(r_B + r_O) \quad (1)$$

is reduced to less than unity, where $< r_A >$ is the average radius of the cation occupying the A-site and $r_B$and r_O are the radii of Fe^{3+} and O^{2-} ions respectively. Continued substitution by Dy^{3+} ions causes further decrease of the tolerance factor as $< r_A >$ reduces to even lower values.

Table 1
The different phases identified from the X-ray diffraction patterns of the samples.

Sample	Phases	Number of peaks indexed	GOF
$BiFeO_3$	$BiFeO_3$ (*R3c*)	21	3.78
$Bi_{0.95}Dy_{0.05}FeO_3$	$BiFeO_3$ (*R3c*)	16	3.98
	$Bi_2Fe_4O_9$ (*Pbam*)	15	
	Bi_2O_3 (*C-4b2*)	1	
$Bi_{0.90}Dy_{0.10}FeO_3$	$BiFeO_3$ (*R3c*)	16	3.94
	$Bi_2Fe_4O_9$ (*Pbam*)	13	
	Bi_2O_3 (*C-4b2*)	1	
$Bi_{0.85}Dy_{0.15}FeO_3$	$BiFeO_3$ (*R3c*)	16	2.35
	$Bi_2Fe_4O_9$ (*Pbam*)	2	
$Bi_{0.80}Dy_{0.20}FeO_3$	$BiFeO_3$ (*R3c*)	16	2.48
	Dy_2O_3 (*Ia-3*)	1	
$Bi_{0.75}Dy_{0.25}FeO_3$	$BiFeO_3$ (*R3c*)	15	4.38
	Dy_2O_3 (*Ia-3*)	2	
	$DyFeO_3$ (*Pnma*)	4	
$Bi_{0.70}Dy_{0.30}FeO_3$	$BiFeO_3$ (*R3c*)	12	9.9
	Dy_2O_3 (*Ia-3*)	3	
	$DyFeO_3$ (*Pnma*)	5	

More importantly, compression forces start to act upon the Fe – O bonds and the Bi^{3+}/Dy^{3+} – O bonds too are subjected to tension. Under such situations, cooperative rotation of oxygen octahedra takes place in order to reduce the lattice stress [24]. Consequently, a lower symmetric orthorhombic structural transformation is induced at $x \geq 0.15$ with concomitant shrinkage in the lattice parameters and in the volume of the unit cell [24,25].

The crystallite size of the $Bi_{1-x}Dy_xFeO_3$ ($x = 0$ to 0.3) samples were calculated using the Debye - Scherrer formula [26].

$$d = \frac{0.9\,\lambda}{\beta \cos\theta} \tag{2}$$

where λ is the wavelength of the X-ray used (Cu*K*α radiation, $\lambda = 1.54$ Å) and β (in radian) is the full width at half maximum (FWHM) of the peak of maximum intensity in the corresponding spectrum. The latter has been corrected for the contribution coming from the instrumental broadening, which was measured on a pure single crystalline Si sample, and then using the relation

$$\beta = \sqrt{\beta^2_{sample} - \beta^2_{instrum}} \tag{3}$$

The results are shown in Fig. 1(h). Non-deletion of the instrumental broadening may underestimate the nanocrystallite sizes, especially for relatively larger ones.

The average crystallite sizes of the samples estimated were in the range 62–9 nm. The crystallite size decreased sharply with increasing Dy^{3+} concentration due to the partial replacement of larger Bi^{3+} ions (ionic radius ≈ 1.17 Å) by smaller Dy^{3+} ions (ionic radius ≈ 0.92 Å) and also due to the suppression of the oxygen ion concentration [23,27]. Likewise, the variation of the unit cell volume with respect to Dy^{3+} ion concentration is shown in Fig. 2. The smaller Dy^{3+} ions lead to a contraction in unit cell volume when substituted in place of the larger Bi^{3+} ions [27].

3.2. TEM studies

Fig. 3(a)-(d) show the HRTEM images of the samples and 3(e)-(h) indicate the lattice fringe widths (*d*-spacing), which correspond to the planes (104), (110), (024), and (012). These values matched well with the *d*-spacing calculated from the SAED patterns given in Fig. 3(i)–(l). It confirms the formation of crystallites with high purity and phase stability in all the samples. The average particle sizes of the samples were calculated using the *IMAGE J* software and Fig. 3(m)–(p) represent the particle size histograms. The average particle sizes obtained for the $Bi_{1-x}Dy_xFeO_3$ ($x = 0$, 0.1, 0.2 and 0.3) samples are 66 nm, 23 nm, 17 nm and 13 nm respectively. The particles showed an inhomogeneous distribution with some of them also agglomerating into larger clusters. It is obvious from this figure that, when the Dy^{3+} concentration increases, the particle sizes decreased and are well matched with the crystallite sizes calculated from the XRD patterns of the same samples.

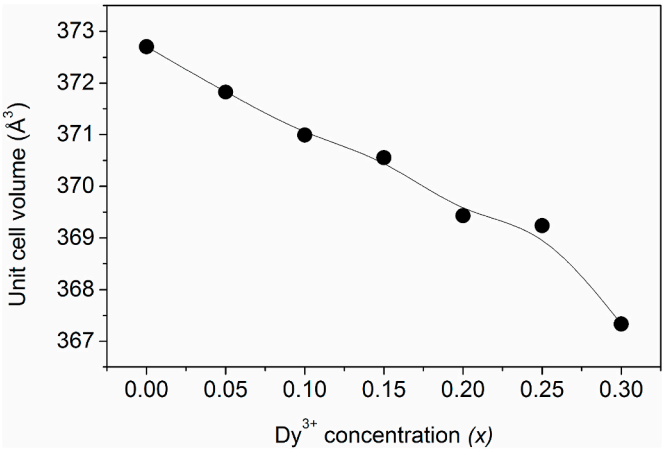

Fig. 2. Unit cell volume of the $Bi_{1-x}Dy_xFeO_3$ ($x = 0$–0.3) samples versus the Dy^{3+} ion concentration (The errors are within the size of the points).

3.3. EDAX analysis

Elemental analysis in substitution studies is utmost essential to judge the extent of success of the process and also holds clue to look for vacancy type defects within the crystallites. The EDAX spectra of $Bi_{1-x}Dy_xFeO_3$ ($x = 0$, 0.1, 0.2 and 0.3) samples are illustrated in Fig. 4. The spectra confirmed the presence of Bi, Dy, Fe, and O in each sample. The EDAX analysis confirmed the success of substitution of Bi^{3+} ions by Dy^{3+} ions in the $Bi_{1-x}Dy_xFeO_3$ samples. The calculated and the experimentally measured atomic percentages of each element in the samples are given in Table 2. While Bi^{3+} and Dy^{3+} ions are found in excess, the concentrations of Fe^{3+} and O^{2-} are conspicuously less in the substituted samples. This is an indication to the presence of defects of both interstitial and vacancy type in the samples. The latter are investigated by positron annihilation, as discussed later, while the interstitial type defects are insensitive to the technique due to the Coulomb repulsion experienced by the positrons by virtue of the positive charge of the ion cores.

3.4. UV–Vis spectroscopy

The optical properties of $Bi_{1-x}Dy_xFeO_3$ ($x = 0$–0.3) samples were studied using diffuse reflectance spectroscopy. It is found that the maximum absorption occurred in the wavelength range 450–550 nm.

The band gap energy of all the samples were calculated from the plot of $(f(R)h\nu)^2$ versus $h\nu$ and are given in Fig. 5, where $f(R)$ indicates the Kubelka - Munk function [28] of *R*, the reflectance and was calculated using the relation

$$f(R) = \frac{(1-R)^2}{2R} \tag{4}$$

The optical band gap energies of the nanocrystalline samples were obtained from the tangents meeting $(f(R)h\nu)^2 = 0$ and the results are given in Fig. 6. The band gap energies of the samples matched with the reported values for pure and Dy^{3+}-doped $BiFeO_3$ [27]. The gradual decrease in the band gap energy with increasing Dy^{3+} concentration is due to the existence of additional energy levels between the valance band and the conduction band (O -*2p* states to Fe -*3d* state) [27] because of which radiation-less transition from the conduction band to these energy levels are prompted before the final de-excitation of the electrons to the valence band.

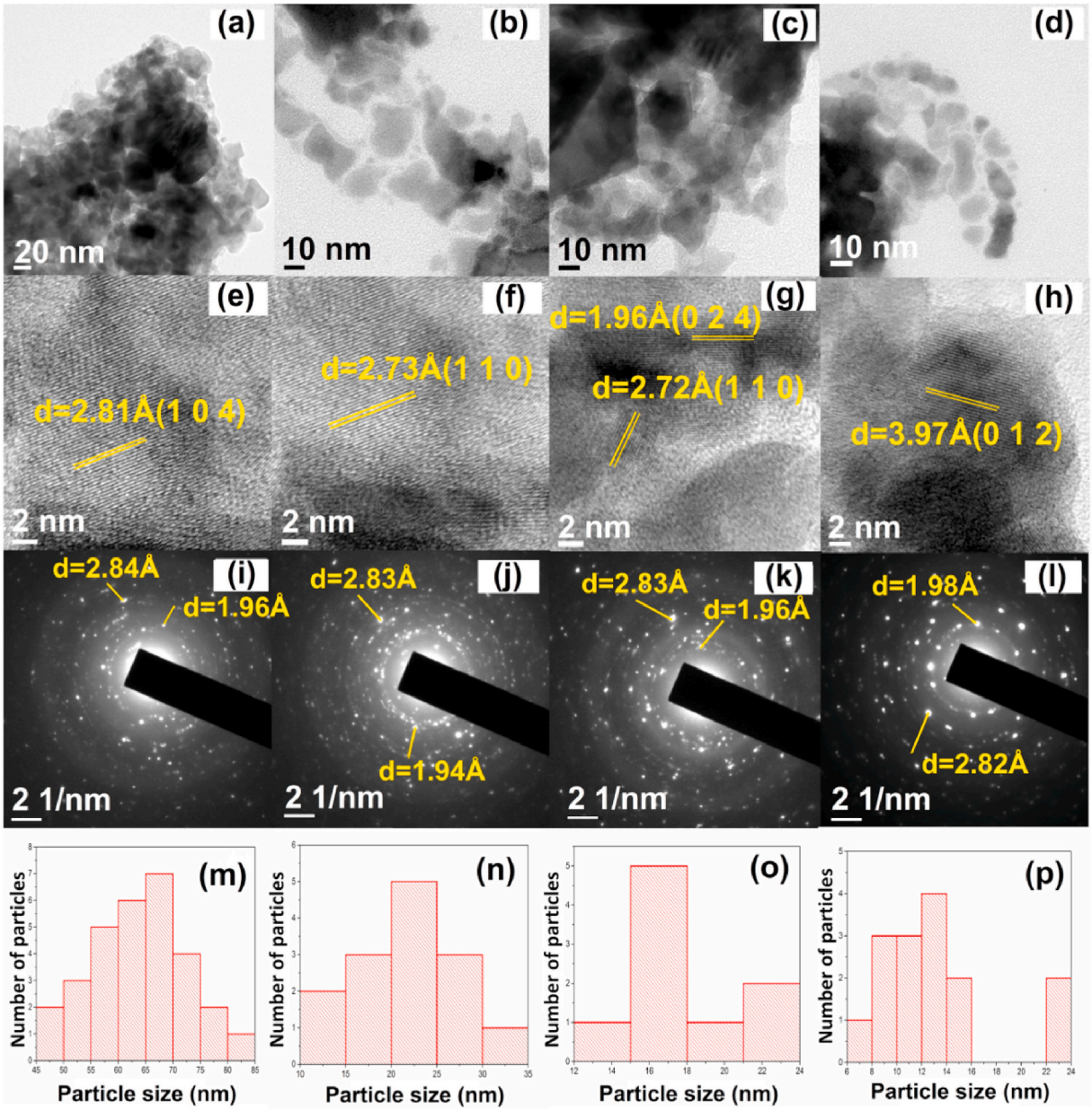

Fig. 3. (a)–(d) TEM images, (e)–(h) HRTEM images, (i)–(l) SAED patterns and (m)–(p) particle size histograms of the $Bi_{1-x}Dy_xFeO_3$ ($x = 0$, 0.1, 0.2 and 0.3) samples.

3.5. Dielectric studies

In furtherance to the understanding of the electrical characteristics of the systems under investigation, the variation of the dielectric constant of the $Bi_{1-x}Dy_xFeO_3$ samples (x = 0–0.3) at room temperature under different frequencies (f) of the applied electric field has been studied in the range $f = 100$ Hz to 2 MHz and the results are shown in Fig. 7. The dielectric constant was calculated using the equation

$$\varepsilon^{'} = C_p\, d / \varepsilon_0\, A \tag{5}$$

where $\varepsilon_0$is the permittivity of free space,$C_p$is the parallel capacitance, d is the thickness of the pellet used for the dielectric measurements and A is the area of its cross section [29].

The dielectric constants of all the samples decrease with increasing frequency of the field and remain constant at frequencies larger than 10 kHz. At lower frequencies, the space charge and the dipolar polarizations are mainly responsible for the dielectric characteristics of a material. In this case, the space charges are created by the vacancies of oxygen (V_0^{2+}) and bismuth (V_{Bi}^{3-}) in the Dy^{3+} doped $Bi_{1-x}Dy_xFeO_3$ samples. These dipoles have sufficient time to

align with the applied electric field at lower frequencies. But at higher frequencies, the electric dipoles cannot follow the rapidly alternating applied field and this leads to incomplete polarization. These observations are in agreement with the phenomenon of dipole relaxation as reported in literature [29–31]. The value of the dielectric constant of each sample at frequency 1 kHz is presented in Fig. 8. It is noted that the value of dielectric constant is found to increase with the increase in Dy^{3+} concentration [32,33]. This is due to the reduction in particle size on Dy^{3+} substitution, resulting in an increase in the dielectric constant. The presence of smaller nanocrystallites at higher concentrations of substitution as shown in Fig. 1(h) and obtained from Fig. 3(m)–(p) acts as a large insulating barrier for mobile charge carriers [34]. When the Dy^{3+} concentration increases up to $x = 0.2$, the dielectric constant increases to 3.6 times the value of the pure sample due to the presence of maximum concentration of the surface defects. With further increase in Dy^{3+} concentration, the dielectric constant shows a tendency

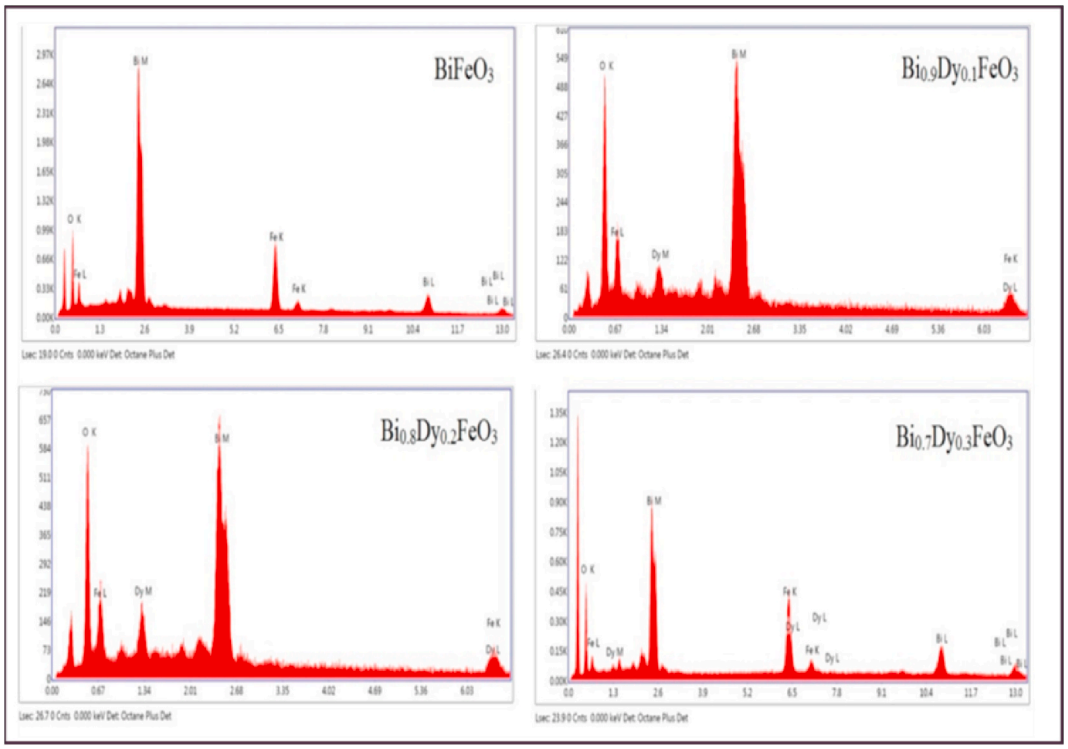

Fig. 4. EDAX spectrum for the $Bi_{1-x}Dy_xFeO_3$ (x = 0, 0.1, 0.2 and 0.3) samples.

Table 2
The atomic percentages of elements of the $Bi_{1-x}Dy_xFeO_3$ (x = 0, 0.1, 0.2 and 0.3) samples calculated from the EDAX spectra.

Sample	Calculated atomic percentage (%)				Measured atomic percentage (%)			
	Bi	Dy	Fe	O	Bi	Dy	Fe	O
$BiFeO_3$	20	0	20	60	20.64	0	19.33	60.03
$Bi_{0.9}Dy_{0.1}FeO_3$	18	2	20	60	18.93	2.40	19.04	59.63
$Bi_{0.8}Dy_{0.2}FeO_3$	16	4	20	60	16.90	4.02	20.03	59.05
$Bi_{0.7}Dy_{0.3}FeO_3$	14	6	20	60	14.73	6.82	19.81	58.64

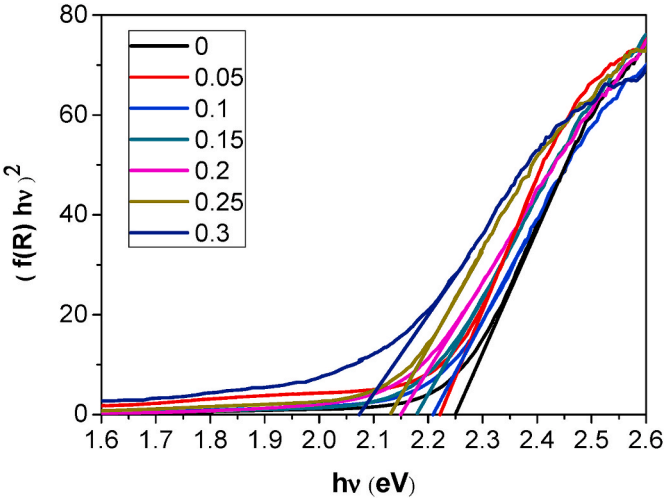

Fig. 5. $(f(R)h\nu)^2$ versus $h\nu$ plot of the $Bi_{1-x}Dy_xFeO_3$ (x = 0–0.3) samples.

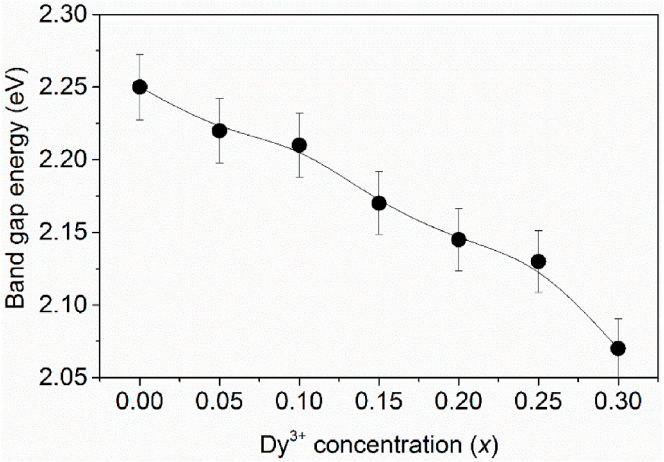

Fig. 6. Band gap energies of the $Bi_{1-x}Dy_xFeO_3$ (x = 0–0.3) samples.

to increase at a reduced rate. It is due to the structural transformation from rhombohedral (*R3c*) to orthorhombic (*Pnma*) phase at higher concentrations ($x > 0.2$) and is explained in terms of the defect analysis in section 3.7.

3.6. Magneto electric coupling

The magneto electric (ME) effect is defined as the dielectric polarization of the material in the presence of an applied magnetic field. A detailed description of the ME coupling experimental procedure can be found in the previous works [35,36]. For performing the ME measurements, the prepared powder samples were pelletized and the electrical contacts on both sides were achieved using silver paint. The measurements have been performed by placing the prepared pellets at the middle of a Helmholtz coil, which is excited with an ac magnetic field (H_{ac}). The reorientation of the electric dipoles within the sample in the

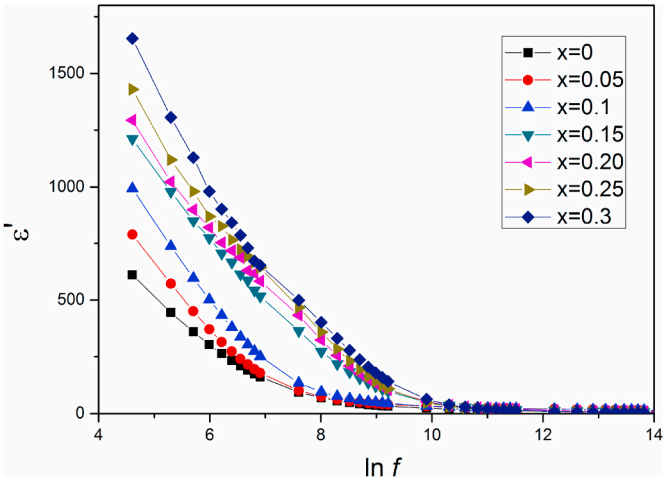

Fig. 7. The dielectric constant versus frequency (of the applied electric field) variation of the $Bi_{1-x}Dy_xFeO_3$ (x = 0–0.3) samples.

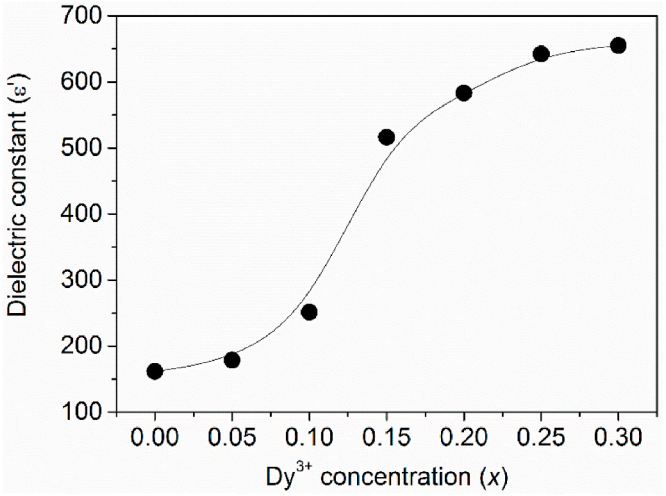

Fig. 8. Dielectric constant of each sample with respect to Dy^{3+} concentration at frequency 1 kHz.

presence of the applied ac magnetic field voltage in the upper and lower surface area of the pellet and this voltage difference was monitored using a lock-in amplifier within the differential setting. This arrangement also helps to avoid the possible errors caused by the induction effect. The measurements have been conducted by varying the ac magnetic field (of frequency 850 Hz) from 0 to 80 Oe in the presence of a constant dc bias magnetic field (H_{dc}) of strength 2 kOe [37].

The electric polarization of $Bi_{1-x}Dy_xFeO_3$ (x = 0–0.3) samples at room temperature was measured under ac magnetic fields using the lock-in amplifier method. Magneto electric coupling gives information on the coexistence of ferroelectric and magnetic phases of the samples. It is defined by the magneto electric voltage coefficient (α_E) [38,39].

$$\alpha_E = dE/dH \tag{6}$$

Fig. 9 represents the dependence of the ME voltage with the strength of the applied ac magnetic field H_{ac} at a fixed frequency of 650 Hz with constant dc bias field of 3.5 kOe. The ME voltage coefficient α_E shows a linear dependence with the frequency and its value determined from the slope of the ME voltage versus H_{ac} curves of Fig. 9 for the different samples are given in Fig. 10.

When the Dy^{3+} ions are replaced by Bi^{3+} ions, the value of α_E is increased and the maximum value of α_E is found to be 0.144 V/cm for

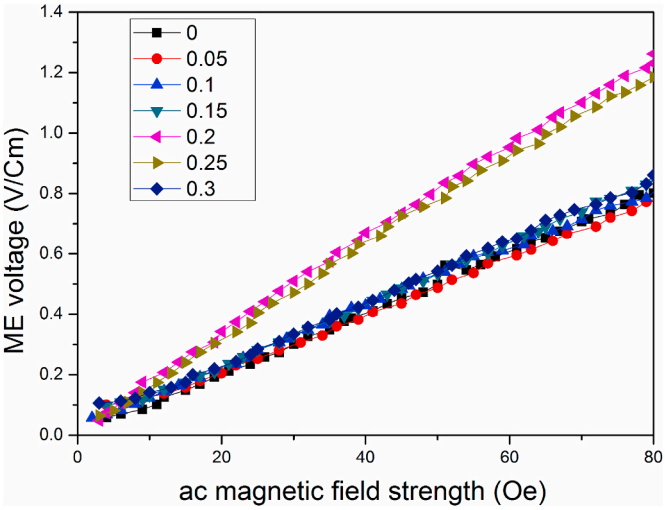

Fig. 9. Magneto electric voltage of the $Bi_{1-x}Dy_xFeO_3$ (x = 0–0.3) samples as a function of the ac magnetic field frequencies at room temperature.

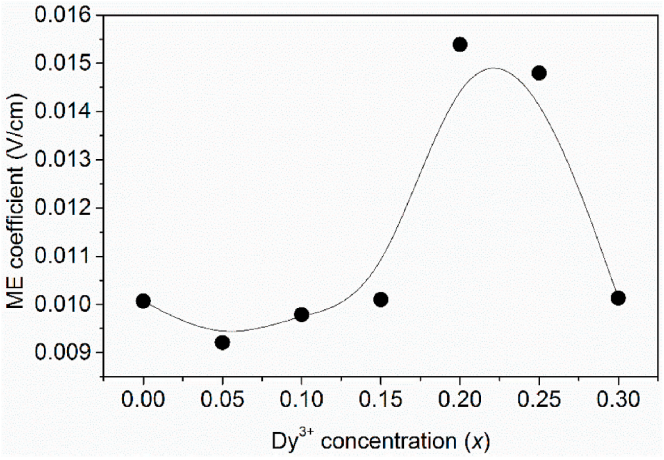

Fig. 10. The ME coupling coefficient (α_E) of the $Bi_{1-x}Dy_xFeO_3$ (x = 0–0.3) samples with different Dy^{3+} concentrations. (The errors are within the size of the points.)

the concentration x = 0.2, after which the coupling coefficient tends to decrease. The maximum value of α_E at x = 0.2 is associated with the ferroelectric and magnetic interaction in the lattice due to the presence of maximum concentration of defects and the structural transformation from rhombohedral (*R3c*) to orthorhombic (*Pnma*) phase at x = 0.2, which is corroborated by the findings of positron annihilation studies discussed in the following section.

3.7. Positron annihilation studies

The significance of defects studies using positrons arises from the above observed anomalies in properties when the structure undergoes a transformation at or above x = 0.2 and also by virtue of the ability of positron annihilation technique to vividly reflect these changes by sensing the evolution and dynamics of the defects rather than the structure itself as in the case of the other more conventional techniques. Defects are inherent in solid systems due to a number of preparatory and thermodynamic conditions as well as because of the non-stoichiometric composition arising out of a number of factors such as charge imbalance and mismatch in ionic radii. It is often realized that substitution is a very effective method of molding the properties of a material for making it better adoptable for various physical and technological applications.

The rationale behind performing positron annihilation spectroscopy (PAS) studies on Dy^{3+}-doped $BiFeO_3$ is threefold, i.e., to understand a mechanism based on defect-engineering and molding to reduce the leakage current density, to explore the possibilities of improvement in ferroelectric properties and to realize a spin-modulated incommensurate structure [18–20]. Since samples are of nanocrystalline composition, positrons can get annihilated at crystallite surfaces and interfaces also [40–42].

Fig. 11 depicts the positron lifetime spectra of the samples where the multi-exponential decay nature of the curves indicates the existence of vacancy type defects in significant concentrations and the variation in their sizes and concentrations with the increasing incorporation of Dy^{3+}. All the data had been analyzed with the well-established software PALSfit, which extracts the individual lifetimes and their corresponding relative intensities after fitting the experimental data to the resolved values with satisfactory reduced chi-square [21]. The three lifetimes τ_1, τ_2 and τ_3 are named in the ascending orders of magnitude of the lifetime values and the corresponding relative intensities as I_1, I_2 and I_3 irrespective of the values.

The intermediate positron lifetime τ_2 and its intensity I_2 are of utmost importance here. It originates from the trapping of positrons in defects, preferentially within the nanocrystallites. Due to the non-occupancy of a number of lattice sites by the designated ions, the ideal stoichiometry is lost after the Dy^{3+} doping and a large number of lattice sites become vacancies and they act as effective trapping centers for positrons. In Fig. 12, which depicts the variation of the positron lifetimes and intensities versus the doping concentration, an abrupt change in the trend of the variation of τ_2 is observed at $x = 0.2$ and it is perceived as due to the transformation of the structure from the distorted rhombohedra (*R*3*c*) to the orthorhombic (*Pnma*) one. This is consistent with the observations from the X-ray diffraction studies in the case of similar substitution studies reported for $BiFeO_3$ by several authors [22,23,43]. In the X-ray diffraction patterns of the present samples shown in Fig. 1, a noticeable deviation in the position of the peaks is observed in the samples with $x > 0.2$, which indicates this transformation. In the intercrystallite regions, where the electron density is significantly low, positronium formation is to be expected although in very small concentrations. Positronium (Ps) is the bound state of the positron with a host electron and gets formed in two ground states, viz., the singlet para-positronium (*p*Ps) and the triplet ortho-positronium (*o*Ps). In condensed matter, the lifetime of *o*Ps gets shortened by a pick-off process involving an electron with opposite spin from the material [44]. The third component τ_3 mainly corresponds to the *o*Ps pick-off lifetime and it is useful in obtaining the magnitudes of the intercrystallite separation and radii of free volume defects, if present [44–46].

The shortest lifetime of τ_1 arises from free annihilation of positrons

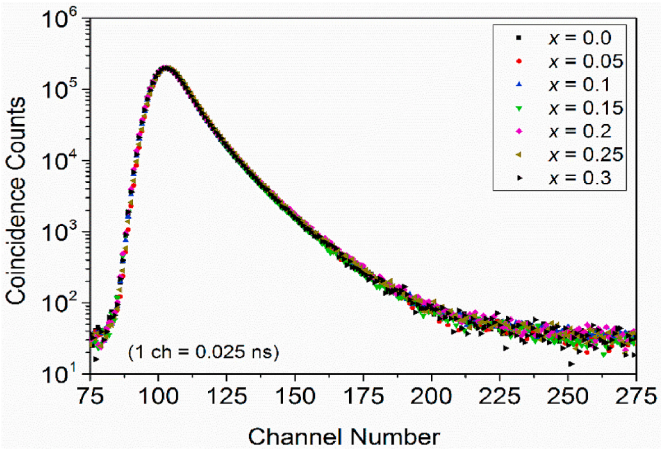

Fig. 11. Peak-normalized positron lifetime spectra of the $Bi_{1-x}Dy_xFeO_3$ (x = 0–0.3) samples.

with the electrons in the bulk regions of the samples along with small percentages ($I_3/3$) of *p*Ps. In this work, I_3 itself is small (<0.3%) and the values of τ_1 are higher than 0.125 ns, the intrinsic lifetime of *p*Ps, and it means Bloch-state diffusion and subsequent trapping of positrons are the main contributors for this component [47].

In a defect-free crystalline solid, the bulk lifetime τ_b is the lifetimes of positrons annihilating within homogeneous electron density region that characterizes the bulk. Since the samples used in this experiment are nanocrystalline in nature, with the average crystallite sizes less than 62 nm in any of the samples, a fraction of the positrons not trapped in defects will diffuse out to the surfaces of the nanocrystallites before annihilation. This happens when the sizes of the crystallites are less than the thermal diffusion length of positrons in materials (~50–100 nm) [48]. In coarse materials where τ_1 represents the admixture of the Bloch-state residence time of the trapped positrons along with those not trapped, τ_1 must be less than τ_b. It follows from the trapping-model based equations wherein the measured positron lifetimes and intensities of the sample containing the defects are related as [47].

$$\frac{1}{\tau_1} = \frac{1}{\tau_b} + \kappa_d \tag{7}$$

and

$$\frac{1}{\tau_b} = \frac{I_1}{\tau_1} + \frac{I_2}{\tau_2} + \frac{I_3}{\tau_3} \tag{8}$$

where κ_d is the positron trapping rate. We also have the mean positron lifetime τ_m defined as,

$$\tau_m = \frac{\tau_1 I_1 + \tau_2 I_2 + \tau_3 I_3}{I_1 + I_2 + I_3} \tag{9}$$

The variation of this parameter is given in Fig. 13 and it gives a cumulative picture of the defect-interaction processes taking place in the samples due to the different doping concentrations. The initial rise of the positron lifetime τ_2 as well as that of τ_m and τ_b is attributable to the replacement (or actual substitution) of Bi^{3+} ions by Dy^{3+} ions since the latter have obvious deficiency of electrons owing to its lower atomic number and the gradual rise of the intensity I_2 depicts an increase in the total defect volume within the samples. The remarkable decrease of these parameters taking place in the samples with $x > 0.2$ is an indication to the closer proximity of the neighboring ions and their electrons to the positron, which can result in this context from a reorientation of the lattice structure and is therefore a confirmation to the rhombohedra to orthorhombic transformation. This is also in conformity with the decrease in average crystalline sizes, lattice parameters and the unit cell volume as depicted earlier in Figs. 1(h) and 2.

Due to the difference in sizes between Bi^{3+} (ionic radius ≈ 1.17 Å) and Dy^{3+} (ionic radius ≈ 0.92 Å) ions, a change in the structural properties of the crystallites compared to the undoped $BiFeO_3$ can be expected since the reduced ionic radii would felicitate a decrease of strain in the crystal lattice and more flexibility for the atoms to move and position among themselves. The incorporation of Dy^{3+} at the Bi^{3+} site is expected to modify the ordering by filling in more vacancies and, in the process, also reducing the number of oxygen vacancies for thermodynamic equilibrium. The reduction in the concentration of oxygen vacancies is not directly reflected by any of the measured positron annihilation parameters and can be only indirectly inferred. Above x = 0.2, a decrease in positron lifetimes owing to the structural transformation is observed. It makes obvious of the fact that Dy^{3+} ions efficiently replace Bi^{3+} ions from their occupied lattice sites during the substitution process and cause structural transformation to take place in the nanocrystallites.

The variations of the different positron lifetimes and intensities show a deviation from the two-state trapping model too [47]. In the undoped sample, large numbers of vacancy type defects of various sizes coexist. The variations of all the three lifetimes justify this argument. In the

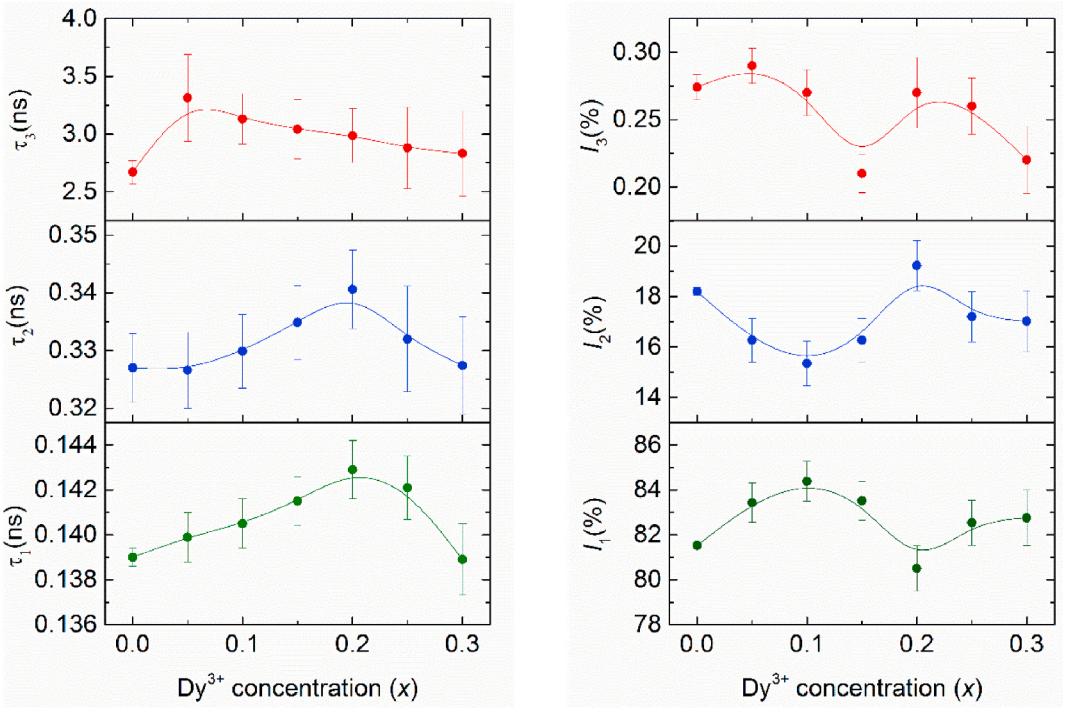

Fig. 12. Plots of positron lifetimes and their relative intensities versus doping concentration of the $Bi_{1-x}Dy_xFeO_3$ (x = 0–0.3) samples.

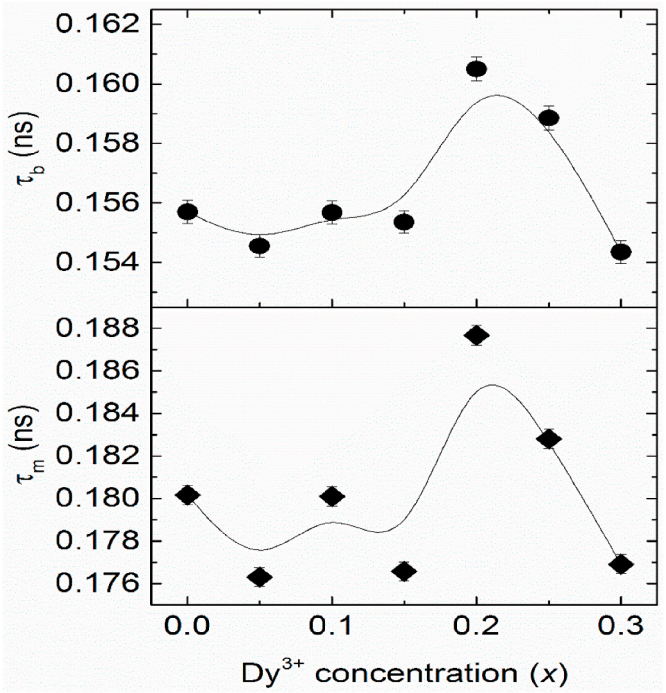

Fig. 13. The variations of the mean positron lifetime (τ_m) and bulk lifetime (τ_b) versus the doping concentrations in the $Bi_{1-x}Dy_xFeO_3$ (x = 0–0.3) samples.

region x = 0.0–0.2, an increase of τ_2 and decrease of I_2 are observed, which signify the elimination of a number of existing vacancies by Dy^{3+} ions. This can be shown from the relation [47].

$$\frac{1}{\tau_1}=\frac{1}{\tau_b}+\frac{I_2}{I_1}\left(\frac{1}{\tau_b}-\frac{1}{\tau_2}\right) \quad (10)$$

The second term on the right hand side is the positron trapping rate κ_d of eq. (7) and eq. (10) necessitates that the bulk lifetime τ_b is a constant for the sample for the model to hold good. The estimation of τ_b for the different samples by using eq. (8) and using the experimental values of the positron lifetimes and intensities however provided varying values and proved the lack of validity of the two-state trapping model and indirectly hinted at the trapping of positrons at the surfaces in addition to the defects within the nanocrystallites. It is noted that there is no significant change in the mean and bulk lifetime as shown up to x = 0.15 but subsequently a sharp rise is observed followed by a decrease at the largest doping concentrations. This is consistent with our previous arguments that a complete redistribution of the ions of the crystallites takes place due to the restructuring transformation. The variations of the mean and bulk positron lifetimes can be thus used in principle to infer qualitative information on the cumulative defect evolution process taking place when the concentration x of substituted Dy^{3+} ions is varied through sequential steps. For example, just before the structural transformation is effected, i.e., between x = 0.1 to 0.2, both the parameters have shown sharp increases, which also coincided with increases in τ_2 and more importantly in I_2 and it indicates an increase in defect volume before the transformation. The decreasing unit cell volume as shown in Fig. 2 should have decreased the positron lifetimes and the above observation is just on the contrary. The reducing sizes of the nanocrystallites with increasing concentrations of substitution (Fig. 1(h)) holds the clue to the diffusion of a fraction of the thermalized positrons to the surfaces of the smaller nanocrystallites. This normally happens when the crystallite sizes reduce to below the thermal diffusion length (l_{th}) of positrons. For $BiFeO_3$, a precise estimation of l_{th} is still not reported but it may be close to ~30 nm, as reported for $SrTiO_3$ [49], which has got an identical perovskite structure. The sizes of the nanocrystallites reduce to less than this limit at x = 0.1 to 0.2, which implies significant number of annihilation events from the surfaces and interfaces of the nanocrystallites. However, the defect-specific positron lifetime is still part of τ_2 and the effects of transformation of the crystallite structure dominate its influence on the absolute magnitudes of τ_2 at $x \geq 0.2$. A model analysis, the details of which we reported in our previous works [18,50–53], in fact implied the reduction of the positron lifetime τ_2 by about 0.030 ns but τ_2 has conspicuously increased at x = 0.1 to 0.2 signifying the annihilation of a considerable number of

positrons at the nanocrystallite surfaces.

The CDBS data acquistion was carried out by recording the two outgoing annihilation gamma ray energies using high resolution HPGe detectors placed on either side of the source-sample assembly. A two parameter spectrum is then generated by taking the sum and difference of the energies in the two coplanar perpendicular axes and distributing the number of events accordingly. A one dimensional projection on to the energy-difference axis of a selected energy-sum window 1.022 ± 0.00145 MeV from the distribution of coincidence events is then generated [54,55]. This represents the actual distribution of Doppler shifts in the annihilation gamma ray energies. Usually, the ratios with respect to that of a reference sample are considered for physical interpretation. The sample chosen as the reference in this case is a pair of pure (99.999%) and well-annealed single crystalline aluminium samples and the ratio curves generated are shown in Fig. 14.

Each ratio curve shows a peak, which develops around the momentum of the electrons predominantly annihilated by the positrons. The peak at p_L (10^{-3} m_0c) = 10.2 in this case arises from positron annihilation with the 2*p* electrons of oxygen ions. This can be explained as due to the trapping of positrons in vacancies created by the absence of the cations, leaving effectively a virtual negative charge to the vacancy region. On the contrary, all the oxygen vacancies which are positively charged will repel positrons. However, very little variations are observed, despite the structural transformation, in either the position or the intensity of the peaks while Dy^{3+} ion concentration is varied through 0.0 to 0.3 and this could be partially due to the insensitivity of positrons to the oxygen ion vacacies. For, in order to sense the changes in cations, positrons are to reside in the positions left vacant by the oxygen ions. Due to the positive charge of the vacancies, positrons are repelled by them and the cationic replacement and redistribution cannot be directly monitored. In spite of these arguments, a well-defined change across x = 0.15 to 0.20 is observed in the variation of the values of the peak ratios of the curves of the different samples when plotted against the content (x) of Dy^{3+} ions in it (Fig. 15). The transformation to the orthorhombic phase is thus once again indicated by this curve and is seen as a reflection of the change in history and position (i.e., site) at which the vacancy type defects are located. Yet another demonstration of the same from the positron annihilation characteristics is to look at the variation of the conventional lineshape parameters *S* and *W* of the CDB spectra (i.e., the projected one-dimensional spectra before the ratio with reference to Al is extrapolated), which are defined from the ratios of the counts within the regions $\Delta E = E_1 - E_2 = \pm$ 0.00058 MeV for *S* and ±0.001885–0.003045 MeV for *W* to the total counts under the respective full spectra extending over $\Delta E = \pm$ 0.00725 MeV [43]. Although not as conspicuous as in Fig. 15, the variations shown in Fig. 16 also reflect changes at x = 0.2 that cannot be overlooked. One point to ponder upon

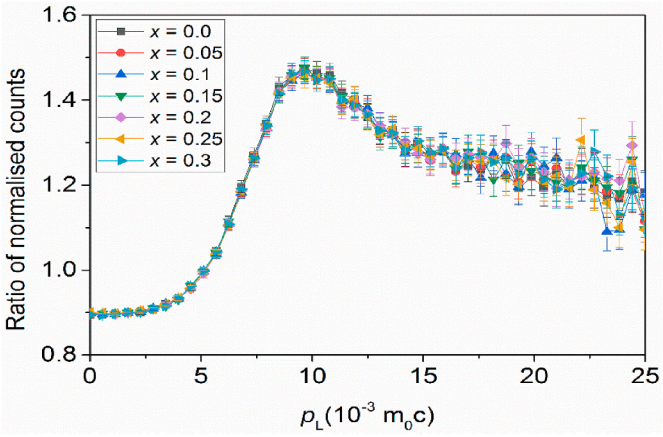

Fig. 14. CDBS quotient spectra of the $Bi_{1-x}Dy_xFeO_3$ samples with respect to the spectrum of reference Al single crystalline samples.

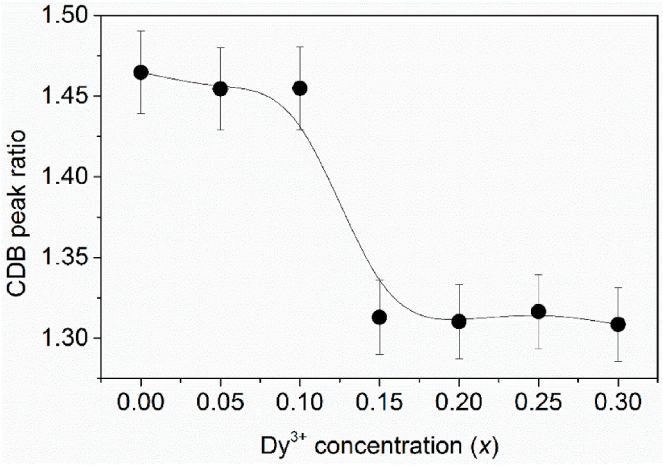

Fig. 15. The variations of the peak ratios of the quotient spectra of Fig. 14 versus the doping concentrations in the $Bi_{1-x}Dy_xFeO_3$ (x = 0–0.3) samples.

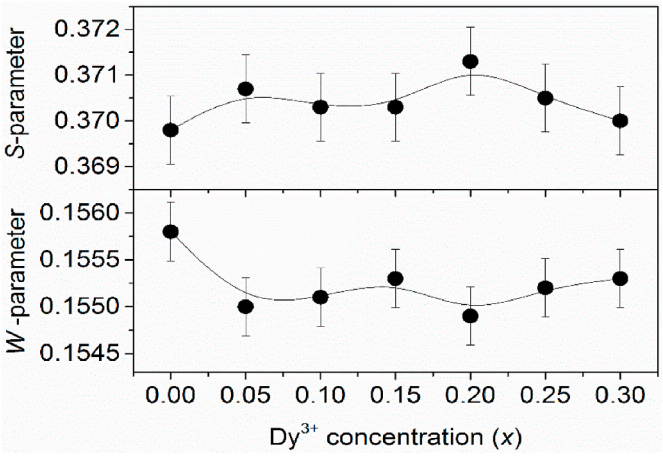

Fig. 16. The variations of the *S*- and the *W*-parameters versus the doping concentrations in the $Bi_{1-x}Dy_xFeO_3$ (x = 0–0.3) samples.

is the fact that the substitution should not result into strain in the lattice as the Dy^{3+} ionic radius is smaller than that of Bi^{3+} and yet the distorted rhombohedral to orthorhombic transformation has occurred and that points towards different mechanism responsible for such a transformation. More studies in this direction are thus required for a deeper insight into the mechanism and driving force behind these changes.

4. Conclusions

In this work, the consequences of doping $BiFeO_3$ with Dy^{3+} are investigated with a motive to infer whether the process may favor the reduction of leakage current and improvement of the polarization and magnetic properties of the multiferroic system. The structural characterization done by X-ray diffraction and the Rietveld analysis of the diffraction patterns showed mixed phases but overwhelmingly indicated a dominant transformation of the main $BiFeO_3$ phase from the rhombohedral (*R3c*) phase to orthorhombic (*Pnma*) phase due to the substitution at x = 0.15–0.20. The deduced sizes of the nanocrystallites and the lattice parameters showed remarkable decreases during the transformation. Further characterization using TEM, HRTEM and EDAX studies all confirmed the nanostructural formation and transformation vividly and the UV–Vis absorption studies showed decreasing band gap energies with increasing doping by Dy^{3+} ions. The drastic increase in dielectric constant (ε') and the maximum value of magneto electric

coupling coefficient (α_E) are obtained at Dy^{3+} concentration $x = 0.2$. This gives a conclusive evidence for the transformation.

Positron annihilation studies confirmed the presence of vacancy type defects in abundant concentrations as expected from the EDAX results, which had indicated marginal deviations from the expected stoichiometries. These defects are essentially the cationic vacancies but with reducing concentrations as the Dy^{3+} ions had radii smaller than that of the Bi^{3+} ions and no strain was formed as a result of occupancy of the sites. The CDBS results also turned out to be further informative as the CDB peak ratio showed a sharp decrease across the structural transformation from the rhombohedral to the orthorhombic phase. The results thus demonstrated that cationic substitution is an effective method to tailor the defect properties of $BiFeO_3$ and can pave the way for the improvement of the multiferroic properties of similar perovskite systems.

CRediT authorship contribution statement

Jincemon Cyriac: Methodology, Formal analysis, Investigation, Writing - original draft. **Saji Augustine:** Conceptualization, Writing - review & editing, Supervision, Project administration. **Nandakumar Kalarikkal:** Resources, Data curation, Supervision. **Shubharaj Mukherjee:** Formal analysis. **Maudud Ahmed:** Formal analysis. **P.M.G. Nambissan:** Investigation, Software, Visualization, Writing - original draft, Supervision.

Declaration of competing interest

The authors declare that they have no known competing financial interests or personal relationships that could have appeared to influence the work reported in this paper.

Acknowledgements

This work was supported by Department of Science and Technology, Government of India (DST – FIST (SR/FST/College- 101/2012)); Jincemon Cyriac acknowledges Mahatma Gandhi University, Kottayam, Kerala for providing financial support through university junior research fellowship (U.O.No.529/A6/2/J. R. F.2018-19/Academic, dated February 02, 2019). The authors are grateful to Dr. Chiranjib Chakrabarti of School of Physics, Huazhong University of Science and Technology, Wuhan, P.R. China for his kind help in performing the Rietveld analysis. They also wish to thank Ms. Vandana G. Kaushik and Ms. Arya Ashok of Amrita Viswa Vidyapeetham, Coimbatore, Tamil Nadu (India) for their help and involvement in the positron annihilation experiments during the tenure of their summer projects in the laboratory at SINP, Kolkata, India.

References

[1] E. Salje, Phase transitions in ferroelastic and co-elastic crystals, Ferroelectrics 104 (1990) 111–120, https://doi.org/10.1080/00150199008223816.
[2] G.A. Smolenskii, I.E. Chupis, Ferroelectromagnets, Sov. Phys. Usp. 25 (1982) 475, https://doi.org/10.1070/PU1982v025n07ABEH004570.
[3] W. Eerenstein, N.D. Mathur, J.F. Scott, Multiferroic and magnetoelectric materials, Nature 442 (2006) 759–765, https://doi.org/10.1038/nature05023.
[4] S. Fusil, V. Garcia, A. Barthélémy, M. Bibes, Magnetoelectric devices for spintronics, Annu. Rev. Mater. Res. 44 (2014) 91–116, https://doi.org/10.1146/annurev-matsci-070813-113315.
[5] A.K. Zvezdin, A.S. Logginov, G.A. Meshkov, A.P. Pyatakov, Multiferroics: promising materials for microelectronics, spintronics, and sensor technique, Bull. Russ. Acad. Sci. Phys. 71 (2007) 1561–1562, https://doi.org/10.3103/S1062873807110263.
[6] P. Swarnakar, L.D. Besra, S. Chatterjee, S. Mukherjee, A. Roy, Designing novel multiferroic perovskite oxide for prospective photovoltaic applications, Mater. Sci. Forum 978 (2020) 353–359, https://doi.org/10.4028/www.scientific.net/MSF.978.353.
[7] D.P. Dutta, B.P. Mandal, R. Naik, G. Lawes, A.K. Tyagi, Magnetic, ferroelectric, and magnetocapacitive properties of sonochemically synthesized Sc-doped $BiFeO_3$ nanoparticles, J. Phys. Chem. C 117 (2013) 2382–2389, https://doi.org/10.1021/jp310710p.
[8] M. Sakar, S. Balakumar, P. Saravanan, S. Bharathkumar, Compliments of confinements: substitution and dimension induced magnetic origin and band-bending mediated photocatalytic enhancements in $Bi_{1-x}Dy_xFeO_3$ particulate and fiber nanostructures, Nanoscale 7 (2015) 10667–10679, https://doi.org/10.1039/C5NR01079A.
[9] C. Madhu, M.B. Bellakki, V. Manivannan, Synthesis and characterization of cation-doped $BiFeO_3$ materials for photocatalytic applications, Indian J. Eng. Mater. Sci. 17 (2010) 131–139. http://nopr.niscair.res.in/handle/123456789/8621.
[10] C. Ponraj, G. Vinitha, J. Daniel, Visible light photocatalytic activity of Mn-doped $BiFeO_3$ nanoparticles, Int. J. Green Energy 17 (2020) 71–83, https://doi.org/10.1080/15435075.2019.1688158.
[11] F. Gao, X.Y. Chen, K.B. Yin, S. Dong, Z.F. Ren, F. Yuan, T. Yu, Z.G. Zou, J.-M. Liu, Visible-Light photocatalytic properties of weak magnetic $BiFeO_3$ nanoparticles, Adv. Mater. 19 (2007) 2889–2892, https://doi.org/10.1002/adma.200602377.
[12] G.S. Lotey, N.K. Verma, Structural, magnetic, and electrical properties of Gd-doped $BiFeO_3$ nanoparticles with reduced particle size, J. Nano Res. 14 (2012) 742, https://doi.org/10.1007/s11051-012-0742-7.
[13] G. Anjum, R. Kumar, S. Mollah, D.K. Shukla, S. Kumar, C.G. Lee, Structural, dielectric, and magnetic properties of $La_{0.8}Bi_{0.2}Fe_{1-x}Mn_xO_3$ ($0.0 \leq x \leq 0.4$) multiferroics, J. Appl. Phys. 107 (2010) 103916, https://doi.org/10.1063/1.3386527.
[14] T. Durga Rao, S. Asthana, Evidence of improved ferroelectric phase stabilization in Nd and Sc co-substituted $BiFeO_3$, J. Appl. Phys. 116 (2014) 164102, https://doi.org/10.1063/1.4898805.
[15] A. Reetu, S. Agarwal, Ashima Sanghi, N. Ahlawat, Structural transformation and improved dielectric and magnetic properties in Ti-substituted $Bi_{0.8}La_{0.2}FeO_3$ multiferroics, J. Phys. D Appl. Phys. 45 (2012) 165001, https://doi.org/10.1088/0022-3727/45/16/165001.
[16] R. Mahesh, P. Venugopal Reddy, A study of ferroelectric and magnetic properties of rare earth (RE=La, Nd, Sm, Gd) doped $BiFeO_3$ using modified Becke Johnson potential with SOC techniques, Mater. Chem. Phys. 232 (2019) 460–470, https://doi.org/10.1016/j.matchemphys.2019.05.012.
[17] K.S. Kumar, S. Ramu, A. Sudharani, M. Ramanadha, G. Murali, R.P. Vijayalakshmi, Enhanced magnetic and dielectric properties of Gd doped $BiFeO_3$: Er nanoparticles synthesized by sol-gel technique, Phys. E Low-dimens. Syst. Nanostruct. 115 (2020) 113689, https://doi.org/10.1016/j.physe.2019.113689.
[18] Jincemon Cyriac, S. Mathew, S. Augustine, P.M.G. Nambissan, Defects characterization studies of europium-substituted bismuth ferrite nanocrystals by positron annihilation and other methods, J. Phys. D Appl. Phys. 51 (2018) 435303, https://doi.org/10.1088/1361-6463/aadfa7.
[19] A. Mukherjee, M. Banerjee, S. Basu, P.M.G. Nambissan, M. Pal, Gadolinium substitution induced defect restructuring in multiferroic $BiFeO_3$: case study by positron annihilation spectroscopy, J. Phys. D Appl. Phys. 46 (2013) 495309, https://doi.org/10.1088/0022-3727/46/49/495309.
[20] Jincemon Cyriac, M.T. Rahul, N. Kalarikkal, P.M.G. Nambissan, Positron annihilation spectroscopic studies of multiferroic $Bi_{1-x}Pr_xFeO_3$ nanocrystalline compounds, J. Phys.: Conf. Ser. 618 (2015), 012012, https://doi.org/10.1088/1742-6596/618/1/012012.
[21] J.V. Olsen, P. Kirkegaard, N.J. Pedersen, M. Eldrup, PALSfit: a new program for the evaluation of positron lifetime spectra, Phys. Status Solidi 4 (2007) 4004–4006, https://doi.org/10.1002/pssc.200675868.
[22] J. Xu, G. Ye, M. Zeng, Structure transition and enhanced multiferroic properties of Dy-doped $BiFeO_3$, J. Alloys Compd. 587 (2014) 308–312, https://doi.org/10.1016/j.jallcom.2013.10.174.
[23] V. Koval, I. Skorvanek, M. Reece, L. Mitoseriu, H. Yan, Effect of dysprosium substitution on crystal structure and physical properties of multiferroic $BiFeO_3$ ceramics, J. Eur. Ceram. Soc. 34 (2014) 641–651, https://doi.org/10.1016/j.jeurceramsoc.2013.10.002.
[24] Xingquan Zhang, Sui Yu, Xianjie Wang, Yang Wang, Zhu Wang, Effect of Eu substitution on the crystal structure and multiferroic properties of $BiFeO_3$, J. Alloys Compd. 507 (2010) 157–161, https://doi.org/10.1016/j.jallcom.2010.07.144.
[25] T. DurgaRao, T. Karthik, Saket Asthana, Investigation of structural, magnetic and optical properties of rare earth substituted bismuth ferrite, J. Rare Earths 31 (4) (2013) 370–375, https://doi.org/10.1016/S1002-0721(12)60288-9.
[26] A.L. Patterson, The scherrer formula for X-ray particle size determination, Phys. Rev. 56 (1939) 978–982, https://doi.org/10.1103/PhysRev.56.978.
[27] P. Chandra Sati, M. Arora, S. Chauhan, M. Kumar, S. Chhoker, Effect of Dy substitution on structural, magnetic and optical properties of $BiFeO_3$ ceramics, J. Phys. Chem. Solid. 75 (2014) 105–108, https://doi.org/10.1016/j.jpcs.2013.09.003.
[28] R. López, R. Gómez, Band-gap energy estimation from diffuse reflectance measurements on sol–gel and commercial TiO_2: a comparative study, J. Sol. Gel Sci. Technol. 61 (2012) 1–7, https://doi.org/10.1007/s10971-011-2582-9.
[29] G.M. Mustafa, S. Atiq, S.K. Abbas, S. Riaz, S. Naseem, Tunable structural and electrical impedance properties of pyrochlores based Nd doped lanthanum zirconate nanoparticles for capacitive applications, Ceram. Int. 44 (2018) 2170–2177, https://doi.org/10.1016/j.ceramint.2017.10.172.
[30] S.K. Abbas, S. Atiq, S. Riaz, S. Naseem, Thermally activated variations in conductivity and activation energy in $SrMnO_3$, J. Mater. Sci. Mater. Electron. 28 (2017) 7171–7176, https://doi.org/10.1007/s10854-017-6397-5.
[31] T. Hussain, S.A. Siddiqi, S. Atiq, M.S. Awan, Induced modifications in the properties of Sr doped $BiFeO_3$ multiferroics, Prog. Nat. Sci.: Materials International 23 (2013) 487–492, https://doi.org/10.1016/j.pnsc.2013.09.004.
[32] P. Uniyal, K.L. Yadav, Observation of the room temperature magnetoelectric effect in Dy-doped $BiFeO_3$, J. Phys. Condens. Matter 21 (2009), 012205, https://doi.org/10.1088/0953-8984/21/1/012205.

[33] G.S. Lotey, N.K. Verma, Phase-dependent multiferroism in Dy-doped $BiFeO_3$ nanowires, Superlattice. Microst. 53 (2013) 184–194, https://doi.org/10.1016/j.spmi.2012.10.005.
[34] R.P. Ummer, P. Sreekanth, B. Raneesh, R. Philip, D. Rouxel, S. Thomas, N. Kalarikkal, Electric, magnetic and optical limiting (short pulse and ultrafast) studies in phase pure $(1-x)BiFeO_3$–$xNaNbO_3$ multiferroic nanocomposite synthesized by the pechini method, RSC Adv. 5 (2015) 67157–67164, https://doi.org/10.1039/C5RA10422J.
[35] B. Raneesh, H. Soumya, J. Philip, S. Thomas, K. Nandakumar, Magnetoelectric properties of multiferroic composites $(1-x)ErMnO_3$–$xY_3Fe_5O_{12}$ at room temperature, J. Alloys Compd. 611 (2014) 381–385, https://doi.org/10.1016/j.jallcom.2014.05.155.
[36] J. Shah, R.K. Kotnala, Induced magnetism and magnetoelectric coupling in ferroelectric $BaTiO_3$ by Cr-doping synthesized by a facile chemical route, J. Mater. Chem. 1 (2013) 8601–8608, https://doi.org/10.1039/c3ta11845b.
[37] Rahul Mundiyaniyil Thankachan, B. Raneesh, Anshida Mayeen, S. Karthika, S. Vivek, S. Swapna, Nair Sabu Thomas, Nandakumar Kalarikkal, Room temperature magnetoelectric coupling effect in $CuFe_2O_4$-$BaTiO_3$ core-shell and nanocomposites, J. Alloys Compd. 731 (2017) 288–296, https://doi.org/10.1016/j.jallcom.2017.09.309.
[38] N. Kumar, A. Gaur, G.D. Varma, Enhanced magnetization and magnetoelectric coupling in hydrogen treated hexagonal $YMnO_3$, J. Alloys Compd. 509 (2011) 1060–1064, https://doi.org/10.1016/j.jallcom.2010.09.181.
[39] C.-W. Nan, M.I. Bichurin, S. Dong, D. Viehland, G. Srinivasan, Multiferroic magnetoelectric composites: historical perspective, status, and future directions, J. Appl. Phys. 103 (2008), 031101, https://doi.org/10.1063/1.2836410.
[40] A. Dupasquier, A.P. Mills, July 6–16, 1993, Lake Como, Villa Monastero, Italy, in: Positron Spectroscopy of Solids – Proceedings of the 125th International School of Physics 'Enrico Fermi', IOS Press, Amsterdam, The Netherlands, 1995, 1–780. Available at, www.iospress.nl/book/positron-spectroscopy-of-solids/.
[41] Tandra Ghoshal, Subhajit Biswas, Soumitra Kar, Subhadra Chaudhuri, P.M. G. Nambissan, Positron annihilation spectroscopic studies of solvothermally synthesized ZnO nanobipyramids and nanoparticles, J. Chem. Phys. 128 (6pp) (2008), 074702, https://doi.org/10.1063/1.2827866.
[42] P.M.G. Nambissan, in: Shishir Sinha, N.K. Navani, J.N. Govil (Eds.), Nanotechnology: Synthesis and Characterization, vol. 2, Studium Press LLC, Houston, U.S.A, 2013, pp. 455–491, ch. 16, www.studiumpress.in/nanotechnology-vol-2-synthesis-andcharacterization.html. Available at.
[43] S. Layek, S. Saha, H.C. Verma, Preparation, structural and magnetic studies on $BiFe_{1-x}Cr_xO_3$ ($x = 0.0$, 0.05 and 0.1) multiferroic nanoparticles, AIP Adv. 3 (2013), 032140, https://doi.org/10.1063/1.4799063.
[44] R.W. Siegel, Positron annihilation spectroscopy, Annu. Rev. Mater. Sci. 10 (1980) 393–425, https://doi.org/10.1146/annurev.ms.10.080180.002141.
[45] R.N. West, Positron studies of condensed matter, Adv. Phys. 22 (1973) 263–383, https://doi.org/10.1080/00018737300101299.
[46] H. Nakanishi, S.J. Wang, Y.C. Jean, Positron Annihilation in Fluids, World Scientific, Singapore, 1988, pp. 292–298.
[47] B. Bergersen, M.J. Stott, The effect of vacancy formation on the temperature dependence of the positron lifetime, Solid State Commun. 7 (1969) 1203–1205, https://doi.org/10.1016/0038-1098(69)90177-X, 17.
[48] R.M. Nieminen, M.J. Manninen, in: P. Hautojarvi (Ed.), Positrons in Solids, Springer Series on Topics in Current Physics vol. 12, Springer, Berlin, Germany, 1979, pp. 145–195, ch. 4.
[49] A. Uedono, K. Shimoyama, M. Kiyoharaabd, K. Yamabe, Defects in CeO_2/$SrTiO_3$ fabricated by automatic feeding epitaxy probed using positron annihilation, J. Appl. Phys. 94 (2003) 5193–5198, https://doi.org/10.1063/1.1606112.
[50] Rahul Mundiyaniyil Thankachan, Jincemon Cyriac, B. Raneesh, Nandakumar Kalarikkal, D. Sanyal, P.M.G. Nambissan, Cr^{3+}-substitution induced structural reconfigurations in the nanocrystalline spinel compound $ZnFe_2O_4$ as revealed from X-ray diffraction, positron annihilation and Mossbauer spectroscopic studies, RSC Adv. 5 (2015) 64966–64975, https://doi.org/10.1039/C5RA04516A.
[51] Jincemon Cyriac, R.M. Thankachan, B. Raneesh, P.M.G. Nambissan, D. Sanyal, N. Kalarikkal, Positron annihilation spectroscopic studies of Mn substitution induced cubic to tetragonal transformation in $ZnFe_{2-x}Mn_xO_4$ ($x = 0.0$–2.0) spinel nanocrystallites, Philos. Mag. A 95 (2015) 4000–4022, https://doi.org/10.1080/14786435.2015.1110631.
[52] Ann Rose Abraham, B. Raneesh, P.M.G. Nambissan, D. Sanyal, Sabu Thomas, Nandakumar Kalarikkal, Defects characterisation and studies of structural properties of sol–gel synthesised $MgFe_2O_4$ nanocrystals through positron annihilation and supportive spectroscopic methods, Phil. Mag. 100 (1) (2019) 32–61, https://doi.org/10.1080/14786435.2019.1668576.
[53] Ann Rose Abraham, B. Raneesh, D. Sanyal, Sabu Thomas, Nandakumar Kalarikkal, P.M.G. Nambissan, Defect-focused analysis of calcium-substitution induced structural transformation of magnesium ferrite nanocrystals, New J. Chem. 44 (2020) 1556–1570, https://doi.org/10.1039/c9nj04068d.
[54] P. Asoka-Kumar, M. Alatalo, V.J. Ghosh, A.C. Kruseman, B. Nielsen, K.G. Lynn, Increased elemental specificity of positron annihilation spectra, Phys. Rev. Lett. 77 (1996) 2097–2100, https://doi.org/10.1103/PhysRevLett.77.2097.
[55] Y. Nagai, T. Nonaka, M. Hasegawa, Y. Kobayashi, C.L. Wang, W. Zheng, C. Zhang, Direct evidence of positron trapping at polar groups in a polymer-blend system, Phys. Rev. B 60 (1999) 11863–11866, https://doi.org/10.1103/PhysRevB.60.11863.